

Northumbria Research Link

Citation: Li, Dongsheng, Zhu, Baoyi, Pang, Kai, Zhang, Qian, Qu, Mengjiao, Liu, Weiting, Fu, Yong Qing and Xie, Jin (2022) Virtual Sensor Array Based on Piezoelectric Cantilever Resonator for Identification of Volatile Organic Compounds. ACS Sensors, 7 (5). pp. 1555-1563. ISSN 2379-3694

Published by: American Chemical Society

URL: <https://doi.org/10.1021/acssensors.2c00442>
<<https://doi.org/10.1021/acssensors.2c00442>>

This version was downloaded from Northumbria Research Link:
<https://nrl.northumbria.ac.uk/id/eprint/49024/>

Northumbria University has developed Northumbria Research Link (NRL) to enable users to access the University's research output. Copyright © and moral rights for items on NRL are retained by the individual author(s) and/or other copyright owners. Single copies of full items can be reproduced, displayed or performed, and given to third parties in any format or medium for personal research or study, educational, or not-for-profit purposes without prior permission or charge, provided the authors, title and full bibliographic details are given, as well as a hyperlink and/or URL to the original metadata page. The content must not be changed in any way. Full items must not be sold commercially in any format or medium without formal permission of the copyright holder. The full policy is available online: <http://nrl.northumbria.ac.uk/policies.html>

This document may differ from the final, published version of the research and has been made available online in accordance with publisher policies. To read and/or cite from the published version of the research, please visit the publisher's website (a subscription may be required.)

Virtual Sensor Array Based on Piezoelectric Cantilever Resonator for Identification of Volatile Organic Compounds

Dongsheng Li¹, Boyi Zhu¹, Kai Pang², Qian Zhang¹, Mengjiao Qu¹, Weiting Liu¹*, YongQing Fu³, and Jin Xie¹*

¹ State Key Laboratory of Fluid Power and Mechatronic Systems, Zhejiang University, Hangzhou, Zhejiang, 310027, P. R. China

² MOE Key Laboratory of Macromolecular Synthesis and Functionalization, Department of Polymer Science and Engineering, Zhejiang University, 38 Zheda Road, Hangzhou 310027, P. R. China

³ Faculty of Engineering and Environment, University of Northumbria, Newcastle upon Tyne NE1 8ST, UK

*Corresponding author. E-mail: liuwt@zju.edu.cn; xiejin@zju.edu.cn

KEYWORDS: *AlN piezoelectric cantilever, Machine learning, Plant diseases diagnosis, Virtual sensor array, VOC identification*

ABSTRACT: Piezoelectric cantilever resonator is one of the most promising platforms for real-time sensing of volatile organic compounds (VOCs). However, it has been a great challenge to eliminate the cross-sensitivity of various VOCs for these cantilever-based VOC sensors. Herein, a virtual sensor array (VSA) is proposed based on a sensing layer of GO film deposited onto an AlN piezoelectric cantilever with five groups of top electrodes for identification of various VOCs. Different groups of top electrodes are applied to obtain high amplitudes of multiple resonance peaks for the cantilever, thus achieving low limit of detections (LODs) to VOCs. Frequency shifts of multiple resonant modes and changes of impedance values are taken as the responses of the proposed VSA to VOCs, and these multi-dimensional responses generate a unique fingerprint for each VOC. Based on machine learning algorithms, the proposed VSA can accurately identify different types of VOCs and mixtures with accuracies of 95.8% and 87.5%, respectively. Furthermore, the VSA has successfully been applied to identify the emissions from healthy plants and “plants with late blight” with an accuracy of 89%. The high levels of identifications show great potentials of the VSA for diagnosis of infectious plant diseases by detecting VOC biomarkers.

Volatile organic compound (VOC) sensors play important roles in many fields such as medical diagnosis, explosive detection, agricultural planting, and pollution monitoring.¹⁻³ Recently, detecting VOCs of biomarkers for diagnosis of infectious plant diseases at their early stages has attracted widespread attention because of its advantages such as non-invasive operation, simplicity, and cost-effectiveness.⁴⁻⁶ For example, Li *et al.* proposed a smartphone-based VOC fingerprinting platform for diagnosis of late blight caused by *Phytophthora infestans*.⁷ As the plant's emission usually consists of multiple gases, the VOC sensors need not only to precisely detect the characteristic VOCs, but also to be able to operate in the presence of various interferences.

VOC sensors developed so far are based on different principles, e.g., semiconductor sensors, optical sensors, field effect transistor devices, and piezoelectric devices.⁸⁻¹⁰ Among them, the piezoelectric cantilever is one of the most prominent real-time VOC detection platforms because of its advantages of fast response, small size and low power consumption, large dynamic range, and quasi-digital output signals.¹¹ Piezoelectric cantilever-based sensors commonly rely on detecting the resonant frequency shifts of a single mode to monitor the VOC concentration, mostly caused by the mass loading effects of the sensing film due to the adsorption of VOCs.¹² This often leads to the poor selectivity of the VOC sensors. Electronic nose (e-nose) system has become a common compromise to enhance the selectivity of VOC sensors,¹³⁻¹⁵ and is usually composed of a sensor array and pattern recognition algorithms such as artificial neural network (ANN) and hierarchical cluster analysis (HCA).¹⁶⁻¹⁸ However, e-nose system has many critical issues such as large volume, high power consumption, and high failure rate, since the breakdown of any component sensor will cause the failure of the whole system.¹⁹

To mitigate the poor selectivity of individual VOC sensor and eliminate these drawbacks of e-noses, virtual sensor array (VSA) has been proposed recently. It is based on the principle that one individual sensor produces multidimensional output vectors similar to those generated from an e-nose.²⁰⁻²² Pattern recognition algorithms are then adopted to process the output vectors for accurate identifications of different VOCs. Recently multiple resonant modes of a single piezoelectric resonator have also been explored to develop VSAs.²³⁻²⁴ However, it is quite commonly reported that some resonant modes of piezoelectric cantilever resonator show low amplitudes of resonance peaks, which leads to a low signal-to-noise ratio (SNR) of the cantilever-based sensors and thus a poor limit of detection (LOD).²⁵ The VOC sensors based on piezoelectric resonators often did not consider the changes of electrical parameters of the sensing film after adsorption of the VOCs, leading to a waste of critical information.²⁶

Typically, a sensing film is deposited on the surface of a VOC sensor, and the properties of this sensing layer greatly affect its responses to VOCs.²⁷ Two-dimensional (2D) materials have attracted extensive research interest for VOCs sensing applications because of their versatile surface chemistry, large specific surface area, and capability of sensitive detection at room temperature.²⁸ For example, MXene-based VOCs sensors were often reported to have ultrahigh signal-to-noise ratios and low limit of detections.¹⁹ However, most 2D materials, such as graphene, MoS₂, and MXene, have good electrical conductivity, which can cause short circuits in micro devices. Among them, graphene oxide (GO) possesses rich surface functional groups, high resistance and good stability, which makes it one of the most promising materials for VOC sensing applications.²⁸⁻³⁰

In this work, as schematically illustrated in **Figure 1**, we propose

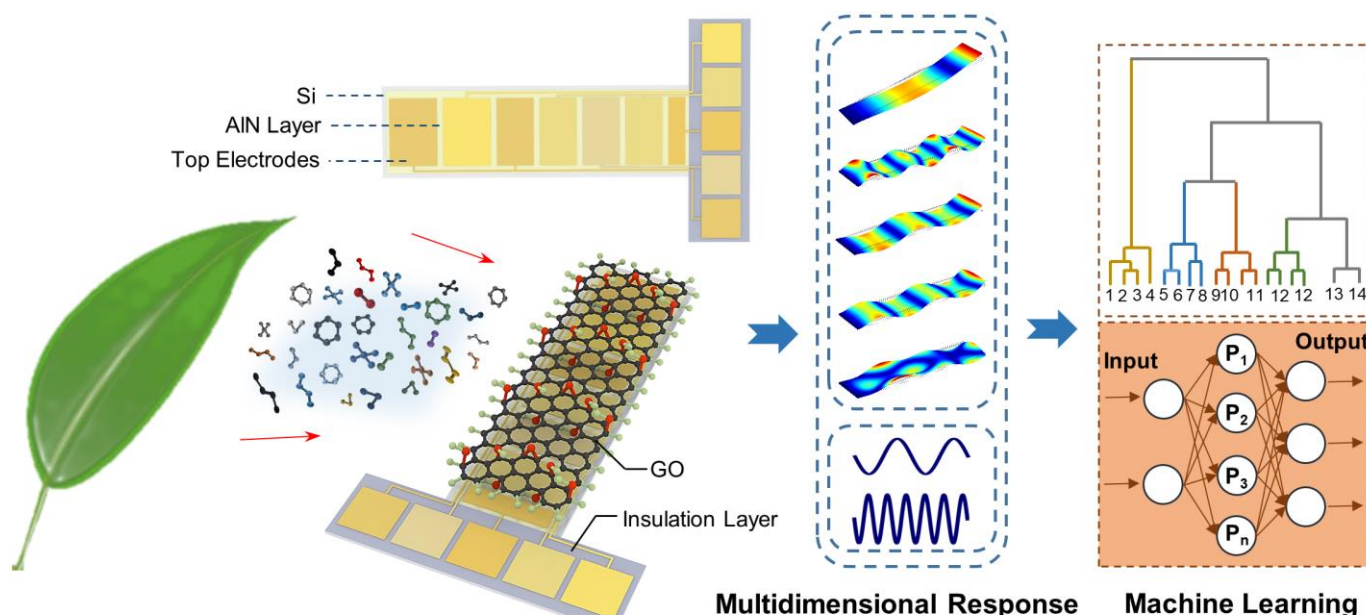


Figure 1. Schematic illustrations of the proposed VSA based on piezoelectric cantilever for plant diseases diagnosis.

a VSA based on an aluminum nitride (AlN) piezoelectric cantilever with five groups of top electrodes for identification of VOCs. Different groups of top electrodes were applied to increase the amplitudes of resonance peaks for multiple modes of the cantilever. The GO film was deposited on the surface of this cantilever to form a VOC sensor, which was then exposed to various VOC concentrations. We applied the frequency shifts of six resonant modes and changes of impedance values at three frequencies between two electrodes as the responses of the proposed VSA to various VOCs. The principal component analysis (PCA), HCA, and ANN were adopted to systematically analyze the VSA's responses for identification of different VOCs. Finally, we successfully demonstrated the identifications of the emissions from healthy plants and "plants with late blight" using the proposed VSA.

EXPERIMENTAL SECTION

Design, Fabrication, and Characterization of the Cantilever-Based VSA. As schematically shown in **Figures 1 and S1**, the proposed VOC sensor is composed of an AlN piezoelectric cantilever and a sensing layer of GO. The area of the cantilever is $300 \times 1000 \mu\text{m}^2$. The top electrode is divided into five groups of electrodes. Different groups of top electrodes are used to increase the amplitude of resonance peaks of multiple modes. The cantilever is composed of an AlN layer on top of a silicon (Si) with their thicknesses of $0.5 \mu\text{m}$ and $10 \mu\text{m}$, respectively. The silicon layer is highly doped and used as bottom electrode. The top electrode consists of 20 nm chrome and 1000 nm aluminum. A thermal oxide layer with a thickness of $0.2 \mu\text{m}$ is used as insulating layer which is between the top and bottom electrodes.

Figure S2 shows the fabrication process of the piezoelectric cantilever. The fabrication process began with a SOI wafer with a highly doped top layer. A thermal oxide layer was firstly grown and patterned using reactive ion etching. AlN layer was sputtering-deposited and patterned by wet etching. Then the top electrodes were deposited and patterned through a lift-off process. The device and handle layers of SOI were patterned by deep reactive ion etching (DRIE) in sequence. GO dispersion was prepared using the modified Hummers' method, as detailed in the literature.^{25, 31} A suspension of GO with a concentration of 0.4 mg ml^{-1} was dropped on the surface of the cantilever to form a sensing layer for VOCs. The cantilever was then dried in a vacuum chamber for 10 mins. Characterization methods of the cantilever-based sensor are detailed in Supporting Information (**S1**).

Process of Finite Element Analysis (FEA) and VOCs Exposure. In order to verify the working principle of the VSA, the FEA simulation was conducted to investigate shifts of multiple resonant frequencies after exposure to two types of VOCs. A three-dimensional (3D) model used in the simulation is shown in **Figure S3**. In the simulation, the density, Young's modulus, and Poisson's ratio of the GO film were set to be 2200 kg m^{-3} , 9 GPa , 0.28 , respectively.^{32, 33} We simulated the changes of the mass and Young's modulus of the sensing film after VOC absorption by changing the density and Young's modulus of the film.

Figure S4 shows the schematic diagram of the experimental setup and details of the chemicals for VOCs sensing, which was detailed in the previous publications.^{26, 27} All the experiments were carried out at 24°C . The VOC sensor was firstly exposed to ethanol (EtOH) with different concentrations from 100 ppm to 800 ppm . The sensitivity, LOD, response and recovery time of the sensor were obtained. In order to investigate the capability of the proposed VSA to identify different VOCs, the sensor was exposed to 100 ppm to 800 ppm of four types of VOCs, i.e., EtOH, methanol (MeOH), acetone, and isopropanol (IPA). In order to test the identification capacity of the proposed VSA to VOC mixtures, the VSA was then exposed to four types of VOC mixtures, i.e., mixtures of EtOH and Acetone (A), EtOH and IPA (B), MeOH and Acetone (C), as well as MeOH and IPA (D), whose concentrations are detailed in **Table S1**.

Furthermore, the VSA was used to identify the emissions from healthy plants and "plants with late blight". We collected 30 emission samples from healthy tomato leaves and 10 emission samples from healthy potato tubers, for a total of 40 samples. Certain amounts of (*E*)-2-hexenal were added to 20 of these samples to ensure that the concentrations of (*E*)-2-hexenal in the samples are from 10 ppm to 20 ppm .⁷ These samples were used to simulate the emissions from "plants with late blight". Then the blind analysis was used to test the identification capability of the VSA for the emissions from healthy plants and "plants with late blight".

Data Analysis Based on Machine Learning Algorithms. Three identical sensors were tested under the same conditions and the results were expressed as the average of the results \pm their standard deviations. In the process of testing the traditional parameters of the VOC sensor, such as sensitivity, LOD, and response time, the frequency shifts of the second-order mode were taken as the responses of the VOC sensor to EtOH, which was centered at 74.8 kHz without the VOC exposure. The LOD of the

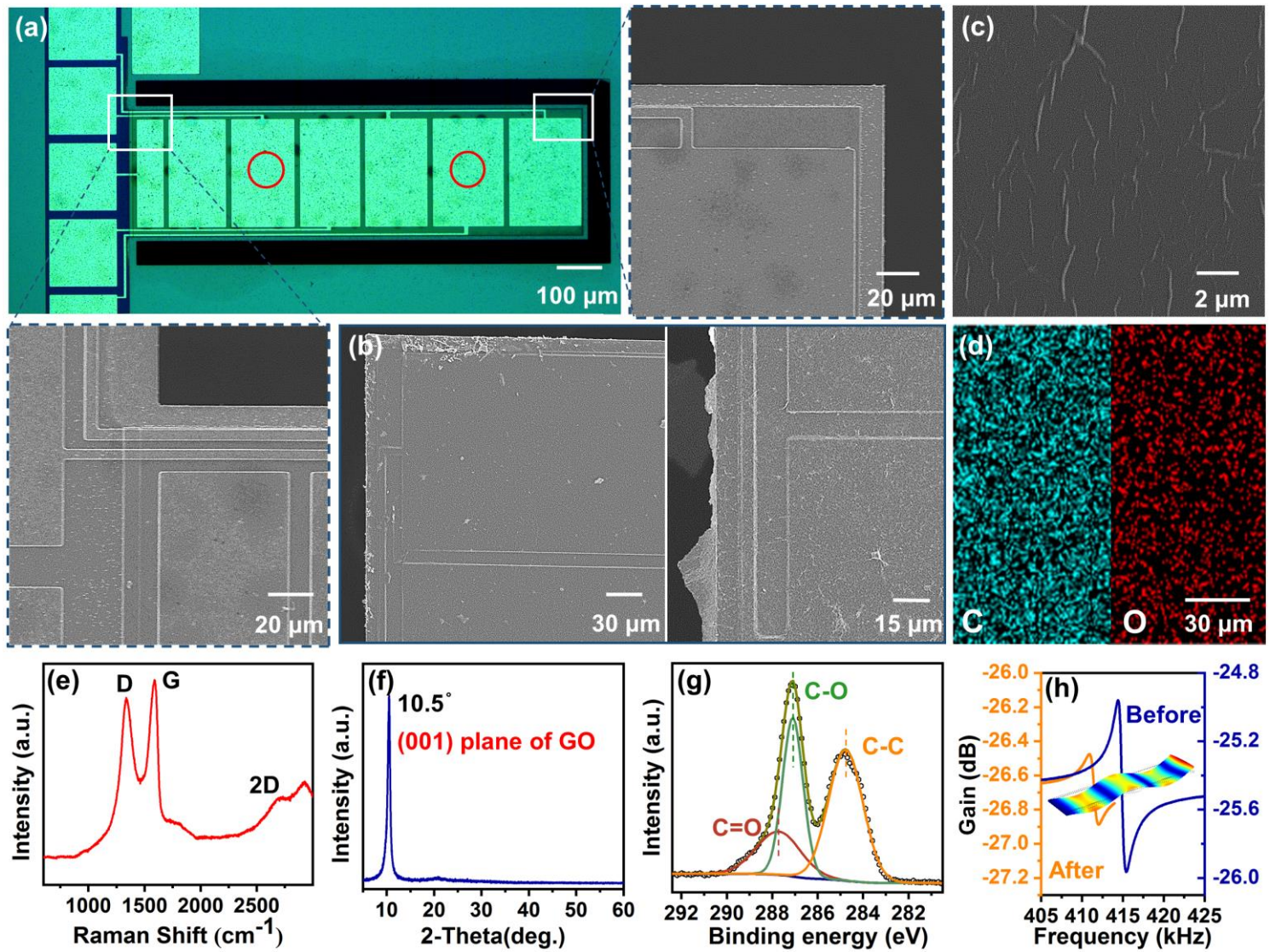


Figure 2. Characterizations of the piezoelectric cantilever-based VOC sensor. Optical and SEM images of the piezoelectric cantilever (a) before and (b) after GO deposition. (c) Surface morphology of the GO film on the cantilever. (d) EDS analysis for elements of C and O. (e) Raman spectrum of the GO film. (f) XRD analysis of the GO film. (g) XPS spectra for C 1s of the GO. (h) Gain curves of the cantilever before and after GO deposition.

sensor to VOCs was calculated by the ratio of three times the standard deviation of the frequency response (3σ) to the sensitivity (S) when the VOCs concentration is zero, i.e., $3\sigma/S$.³⁴ Response time and recovery time were defined as the time to reach 90% of the maximum response and decrease to 10% of the maximum response, respectively.³⁵

The frequency shifts of six resonant modes (Δf_n) and relative changes of the impedance values at three frequencies between the two electrodes ($\Delta Z_n/Z_n$) of the cantilever-based sensor were applied as the responses of VSA to VOCs. **Table S2** shows the details of the nine selected parameters. The six adopted resonant modes are centered at 74.8 kHz (Mode 2, i.e., second-order mode), 211 kHz (Mode 3), 414.9 kHz (Mode 4), 990 kHz (Mode 6), 1.036 MHz (Mode 6'), 1.465 MHz (Mode 7), respectively. Among them, the resonant mode centered at 1.036 MHz is the torsional mode of the cantilever. Because the vibration shape and frequency of the mode are close to the sixth-order mode, as shown in Table S2, it is called "Mode 6". The adopted frequencies of the impedance between the two electrodes marked by the red circle shown in Figure 2a are 1 kHz, 100 kHz, and 1.1 MHz, respectively, which are away from the resonant frequencies of the sensor.

Firstly, PCA was performed on the responses of the VSA to evaluate the dimension of the responses to multiple VOCs and identify different VOCs qualitatively. Then the obtained principal components (PCs) were input to HCA, one of the unsupervised machine learning methods, to identify different VOCs quantitatively. The VSA's responses to the VOCs were input to an

ANN model for the supervised classification. To avoid the error of the training model caused by a small amount of the data set, the Synthetic Minority Over-sampling Technique (SMOTE) method was employed to amplify the data set. Both the hold-out method and leave-one-out cross validation (LOOCV) method were used to evaluate the performance of the trained model. Details of these machine learning algorithms are shown in S2 in the Supporting Information.

RESULTS AND DISCUSSION

Characterization of the Fabricated Cantilever-Based Sensor. The proposed VOC sensor is composed of an AlN piezoelectric cantilever and a sensing layer of GO. **Figures 2a, 2b,** and **S5** show the optical and scanning electron microscope (SEM) images of the piezoelectric cantilever before and after GO deposition. As shown in Figures 2b and S5c, a uniform GO layer is formed on the surface of the cantilever. Surface morphology of the GO film on the cantilever is shown in **Figures S6** and **2c**, which reveal a uniform GO film with some folds. Energy dispersive X-ray spectroscopy (EDS) analysis of the GO film is shown in **Figure 2d**. The elements of C and O are evenly distributed across the entire film. As shown in **Figure 2e**, two main peaks corresponding to the first-order D peak (1340 cm^{-1}) and G peak (1590 cm^{-1}) appear in the Raman spectrum of GO, indicating the existence of numerous structural defects because of the rich chemical functionalization of GO.³⁶ As shown in **Figure 2f**, X-ray diffraction (XRD) curve of the GO film reveals a sharp peak at $2\theta = 10.5^\circ$, indicating the interlayer

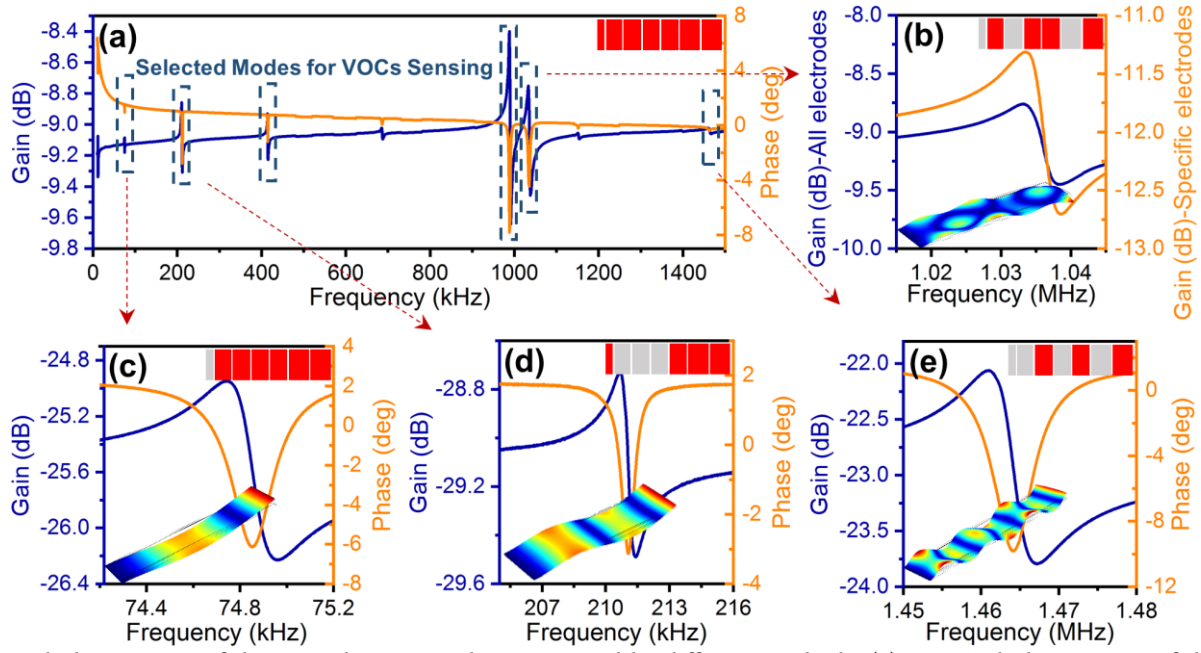


Figure 3. Gain and phase curves of the piezoelectric cantilever activated by different methods. (a) Gain and phase curves of the piezoelectric cantilever activated by all top electrodes (i.e., conventional design for piezoelectric cantilever). (b) Comparison for gain curves of the cantilever activated by different methods. (c-e) Gain and phase curves of the cantilever operated at various modes activated by specific groups of top electrodes.

spacing of the GO film is 8.8 Å.³⁷ Figure 2g shows the C 1s spectrum of X-ray photoelectron spectroscopy (XPS) for the GO film. The C 1s spectrum can be deconvoluted into three peaks centered at 284.8, 287.1, and 287.8 eV. They are corresponding to chemical bonds of C-C, C-O, and C=O on the surface,³⁸ respectively, indicating the existence of rich surface functional groups. Figures S7a, 2h, and S7b show the gain and phase curves of the piezoelectric cantilever operated at the second-order, fourth-order, and seventh-order modes before and after GO deposition, respectively. The resonant frequencies of the cantilever are reduced due to the mass loading effect caused by the deposition of GO film.

Working Principle of the VSA Based on Piezoelectric Cantilever. Typically, the cantilever is excited by one single top electrode and the piezoelectric stress produced by this method effectively matches the vibration shape of the first-order mode. In this case, the piezoelectric stress does positive work on the cantilever. However, when the cantilever works in higher-order modes, the piezoelectric stress generated by a single top electrode no longer matches the vibration pattern. Part of the piezoelectric stress will impede the vibration of the cantilever, which leads to an inefficient electromechanical transduction and thus a low amplitude of the resonance peak.^{39, 40} In this study, the top electrode was divided into five groups and different groups of top electrodes were adopted for matching the vibration shapes of multiple modes. In this way, the amplitudes of resonance peaks for the multiple modes were all increased.

Figure 3a shows the gain and phase curves of the fabricated cantilever activated by all top electrodes (i.e., conventional design for piezoelectric cantilever) within a frequency range from 0 to 1.5 MHz. Some modes of the piezoelectric cantilever resonator show low amplitudes of resonance peaks. Figures 3b and S8a show the comparisons for gain and phase curves of the cantilever activated by specific groups of top electrodes and all top electrodes within a frequency range from 1.02 MHz to 1.05 MHz, respectively. The excitation electrodes and corresponding vibration pattern are shown in the corners of Figure 3b. The amplitude of the resonant peak of the cantilever operated at around 1.036 MHz is improved by applying specific groups of top electrodes. Figures 3c-e and S8b&c show the gain and phase curves of the cantilever operated at various modes activated by specific groups of top electrodes.

Table S3 shows peak-to-peak values of the resonance peaks for multiple modes in the gain curves of the cantilever activated by specific electrodes and all top electrodes. The amplitudes of these resonant peaks are significantly increased by applying specific groups of top electrodes.

The VOC adsorption mechanism of the GO film is relevant to both the functional groups and defects of the GO layer.^{41, 42} Some VOCs are adsorbed by the defects of the GO nanosheets, while some VOCs interact with surface functional groups of GO, e. g., -OH and -O. Moreover, VOC molecules can intercalate into GO interlayers and thus increase the spacing among layers of the GO film, causing the changes of elastic modulus of the GO film.⁴³ Changes in both the mass and elastic modulus of the GO film will lead to frequency shifts of the cantilever resonator-based sensor. The change ratios for the mass and elastic modulus of the GO film caused by various VOCs are quite different.⁴⁴ Ratios of resonant frequency shifts of multiple resonant modes caused by the changes in mass and elastic modulus of the film are also different. Therefore, each VOC leads to a unique ratio of frequency shifts of multiple resonant modes, which can be applied as the fundamental principle of the VSA.

FEA simulation was performed to prove the above assumptions. In the simulation, two types of VOCs lead to different ratios of changes in mass and elastic modulus of the GO film. VOC 1 causes only a one tenth change in the mass of the film, while VOC 2 causes a one tenth change in both the mass and modulus of elasticity. Table S4 shows the resonant frequencies of multiple modes after exposure to two types of VOCs. Figures 4a and 4b show the ratios of the relative frequency shifts of multiple modes to that of the first-order mode for the cantilever, i.e., $\Delta f_n/f_n/(\Delta f_1/f_1)$. Two types of VOCs lead to different ratios of frequency shifts of multiple resonant modes. Therefore, frequency shifts of multiple resonant modes can be applied for identification of multiple VOCs using the cantilever-based sensor. Furthermore, the adsorption of VOCs also causes impedance changes of the sensing film, which is often applied for VOC identifications.²⁷ To avoid the waste of information, changes of the impedance values at multiple frequencies were also used for VOC identifications.

Sensing Parameters of the VOC Sensor to Ethanol. The VOC sensor was firstly exposed to ethanol with different

concentrations from 100 ppm to 800 ppm. The frequency shifts of the second-order mode were taken as the responses of the VOC

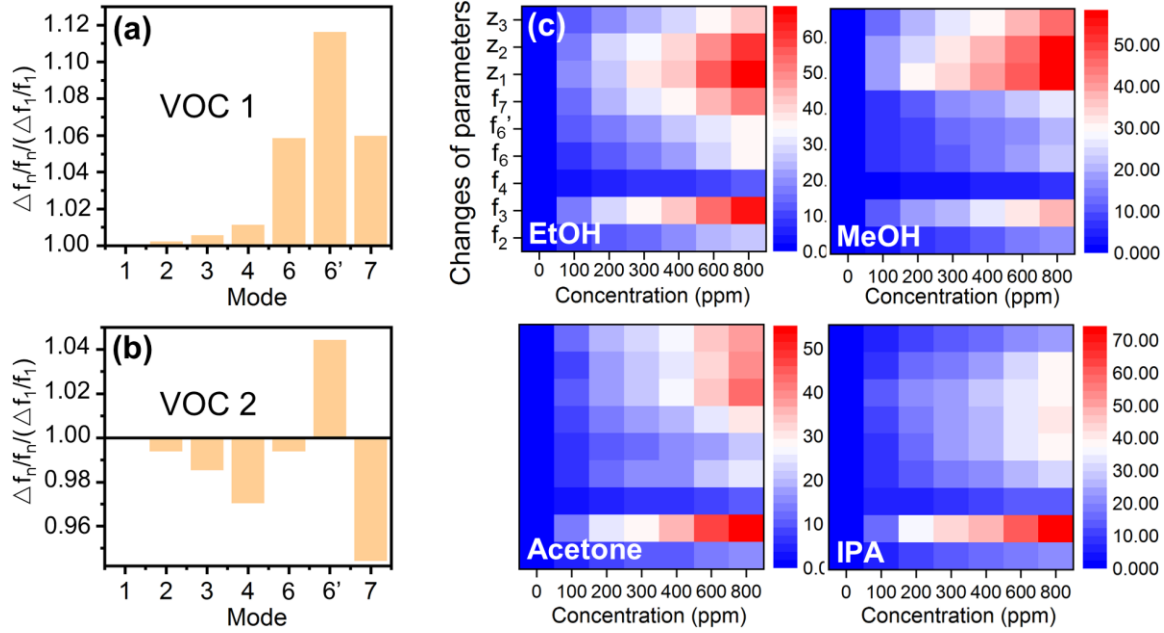


Figure 4. Simulation and experimental fingerprints for multiple VOCs. Ratios of the relative frequency shift of multiple modes to that of the first-order mode after exposure to (a) VOC 1 and (b) VOC 2 by simulation. (c) Experimental VOC fingerprint for four types of VOCs.

sensor to ethanol. **Figure S9** shows responses of the cantilever-based sensor to ethanol. The frequency shift of the sensor vs. the change of ethanol concentration is not linear and the sensitivity is much higher when the ethanol concentration is low. The average sensitivity in the range of ethanol concentration from 0 to 100 ppm was taken as the sensitivity when the ethanol concentration was near zero. **Figures S10a** and **S10b** show the fluctuations of the second-order resonant frequency of the sensor activated by specific groups of top electrodes and all top electrodes when the ethanol concentration is 0, respectively. The noise level has been significantly reduced by applying specific electrodes. The LODs of the sensor to ethanol activated by the two methods are 25.1 ppm and 111.4 ppm respectively. The LOD of the sensor is improved with the enhancement of SNR because of the improvement of the amplitude of the resonant peak.

As shown in **Figure S11a**, the frequency shifts of the proposed VOC sensor were recorded with a time interval of 1 s when the ethanol concentration was changed between 0 and 100 ppm for three cycles. A good repeatability was obtained. **Figures S11b** and **S11c** show that the response and recovery times of the VOC sensor to ethanol are 27 s and 23 s, respectively, indicating its fast responses and great potentials for high-speed VOC detections.

In order to explore the influence of humidity and temperature on the sensor performance, the sensor was firstly exposed to different humidity from 0.1%RH to 90%RH. **Figure S12a** shows the frequency shifts of the sensor vs. the changes of relative humidity. Since the GO film has the capability to adsorb water molecules, changes in humidity cause frequency shifts of the sensor.²⁵ Then we tested the response of the sensor to 100 ppm ethanol in 10%RH, 30%RH and 50%RH, respectively, as shown in **Figure S12b**. Changes in humidity do not greatly affect the response of the sensor to ethanol, i.e., the sensitivity of the sensor. However, the noise level of the sensor increases with the increase of humidity. **Figures S12c** and **S12d** show the fluctuations of the second-order resonant frequency of the sensor in 10%RH and 50%RH when the ethanol concentration is zero, respectively. The LODs of the sensor to ethanol in 10%RH, 30%RH, and 50%RH are 30 ppm, 35.2 ppm, and 39 ppm, respectively. The temperature coefficient of frequency (TCF) is usually used to characterize the influence of temperature on resonator-based sensors.¹⁰ TCF is defined as the ratio of relative frequency shift to temperature change, i.e., $\Delta f/f_0 \Delta T$. **Figure S12e**

shows the relationship between resonant frequency of the sensor and temperature, revealing a linear relationship ($R^2 > 0.99$). The TCF of the sensor is $-20.4 \text{ ppm}/^\circ\text{C}$, which is smaller than other devices as listed in **Table S5**.

Identification of Multiple VOCs. In order to investigate the capability of the proposed VSA to identify different VOCs, the sensor was exposed to 100 ppm to 800 ppm of four types of VOCs. We applied the frequency shifts of six resonant modes (Δf_n) and relative changes of the impedances at three frequencies ($\Delta Z_n/Z_n$) of the cantilever-based sensor as the responses of the VSA, as detailed in the experimental section. **Figure S13** shows the absolute values of the responses of the VSA ($\Delta f_2 - \Delta f_7$ and $\Delta Z_1/Z_1 - \Delta Z_3/Z_3$) to the four VOCs. The resonant frequencies and impedances decrease with the increase of the VOCs' concentration. The VSA's responses are not linear to the changes of the VOCs' concentration. For a better visualization, the responses of the VSA were plotted as heatmaps as the fingerprint of the four VOCs, as shown in **Figure 4c**, in which the units of $\Delta f_2 - \Delta f_7$, $\Delta f_4 - \Delta f_7$, and $\Delta Z_1/Z_1 - \Delta Z_3/Z_3$ were Hz, 10 Hz, and 0.1%, respectively. Apparently, various VOCs have distinct fingerprints, which can be used for direct identification of the VOCs.

In order to evaluate the dimension of the responses to VOCs and identify different VOCs qualitatively, PCA was then performed on the responses of the VSA. **Figure 5a** shows the 3D plots of PCA results for PC1-PC3. The variance shares of the first three PCs are 71.4%, 20.5%, and 6.88%, respectively, accounting for 99% of the total variance. This result confirms that the response of the VSA is a multidimensional output. In **Figure 5a**, different concentrations of the same VOC are represented by points of the same color. Different colored points representing different VOCs are spread out in a 3D space. We performed multivariate linear fitting for PC1-PC3 versus VOCs' concentration using a least square method. The multivariate fitting results are listed as **Equation 1-4**,

$$\varphi_M = 1575.3 + 792.6 * PC1 - 717.3 * PC2 + 118 * PC3 \quad (1)$$

$$\varphi_E = 544.5 + 129.9 * PC1 + 306.1 * PC2 + 226 * PC3 \quad (2)$$

$$\varphi_a = 683.6 + 591.7 * PC1 - 1000.4 * PC2 - 51.1 * PC3 \quad (3)$$

$$\varphi_I = 1024.5 + 461.6 * PC1 + 523 * PC2 - 142 * PC3 \quad (4)$$

in which φ_M , φ_E , φ_a , and φ_I are the predicted concentrations of MeOH, EtOH, acetone, and IPA (ppm), respectively. **Figures 5b&c** and **S14a&b** show the fitting results for EtOH, MeOH, acetone, and

IPA, respectively. The predicted concentrations are very close to the actual concentrations. The adjusted R^2 ($adj. R^2$) of the fittings

for the four VOCs are 0.999, 0.988, 0.986, 0.998, respectively, indicating a good linearity of the VSA's response to VOCs in a

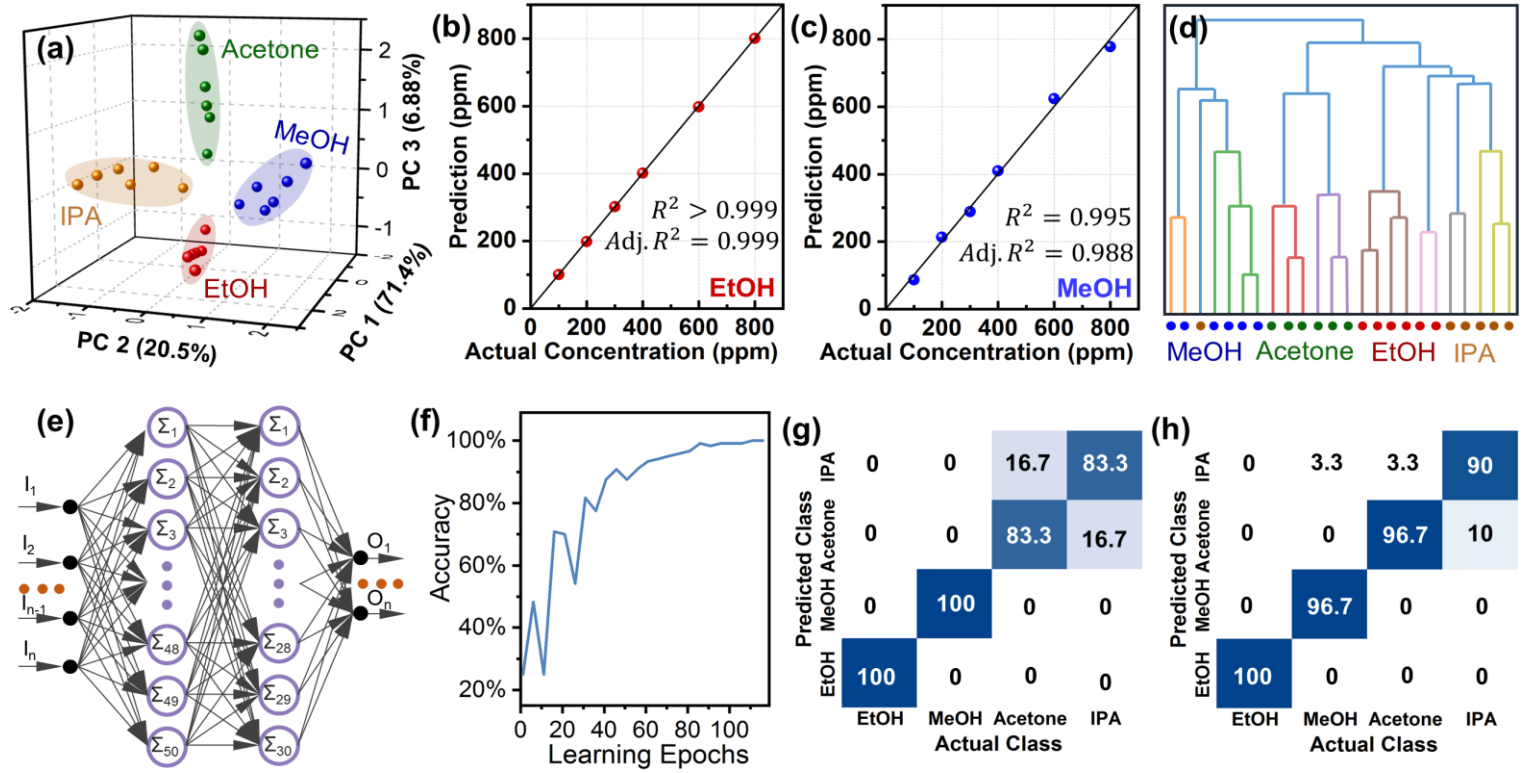


Figure 5. Detection and identification of multiple VOCs. (a) 3D plot for the first three PCs of PCA results. Concentration predictions for (b) EtOH and (c) MeOH by multivariate linear fitting. (d) HCA results for the responses to the four VOCs. (e) Schematic diagram of the adopted ANN model. (f) Learning curve of the ANN model for the amplified data set. LOOCV results of the identifications by the ANN model for the (g) raw data set and (h) amplified data set.

multidimensional space.

The data of PC1- PC3 were then input to HCA for quantitative and unsupervised classifications of various VOCs. **Figure 5d** shows the HCA results for the responses of four VOCs, indicating an accuracy of 87.5% for identification of the four VOCs. An ANN model composed of two linear layers was adopted for supervised classifications. As shown in **Figure 5e**, the first linear layer consists of 50 nodes, while the other layer consists of 30 nodes. These layers are fully connected. To avoid the accidental errors caused by a small amount of the data set, we amplified the data 5 times from 24 (four types of VOCs with six concentrations) to 120 data points using the SMOTE method. **Figures 5i** and **5f** show the learning curves of the ANN model using the raw data set and the amplified data set, respectively. After 100 learning epochs, the accuracy of the model does not apparently increase with the increase of learning epochs. We then randomly divided the amplified data set into a training set and a test set, containing 90 and 30 data, respectively. After 100 times of training based on the training set, the classification accuracy using the ANN model for the test set is 90%. **Figures 5h** and **5g** show the LOOCV results of the VOCs identifications using the ANN model for the raw data set and the amplified data set, indicating their validation accuracies of 91.6% and 95.8%, respectively. Therefore, different VOCs can be accurately identified using the piezoelectric cantilever-based sensor and ANN model. **Figures S16a-e** show the cross validation results for VOCs identifications based on other machine learning algorithms, i.e., support vector machine, naive Bayes, Markov chain, decision tree, and gradient-boosted trees, respectively. The corresponding validation accuracies are 70.8%, 16.7%, 4.2%, 20.8%, and 20.8%, respectively. Among these methods, the ANN model is the most suitable one for VOCs identification using the proposed VSA.

Identifications of VOC Mixtures for Diagnosis of Plant Diseases. The plant emission generally consists of multiple VOCs. In order to test the identification capacity of the proposed VSA to

VOC mixtures, the VSA was exposed to four types of VOC mixtures. **Figure S17** shows the 3D plot of PCA results for responses to VOCs mixtures. Points with different colors represent different VOC mixtures and they are spread out in a 3D space. The data of PC1- PC3 were then input to the HCA for quantitative identifications of VOC mixtures. **Figure S18** shows the identification results for the responses to various VOC mixtures, revealing an accuracy of 79.2% using the HCA method. The ANN model was further adopted for supervised classifications of VOC mixtures and the raw data set was amplified by 5 times from 24 (four types \times six concentrations) to 120 data points using the SMOTE method. **Figures 6a** and **6b** show the cross validation results of the mixtures identifications based on the ANN model for the raw data set and amplified data set using the LOOCV method, showing the validation accuracies of 83.3% and 87.5%, respectively. **Figures S19a-e** show the LOOCV results for the identifications using other machine learning algorithms, i.e., support vector machine, naive Bayes, Markov chain, decision tree, and gradient-boosted trees, respectively. The corresponding validation accuracies are 25%, 4.2%, 12.5%, 5%, and 25%, respectively. Among these methods, the ANN model is the most suitable one for identifications of VOCs mixtures.

Then the proposed VSA was applied to distinguish the “plants with late blight” from the healthy plants by detecting the biomarkers in their emissions. The VSA was firstly exposed to (*E*)-2-hexenal from 10 ppm to 80 ppm, which is one of the biomarkers of VOCs for late blight.⁷ **Figures S20** and **6c** show the absolute values of responses of the VSA to (*E*)-2-hexenal, in which the units of $\Delta f_2 - \Delta f_4$, $\Delta f_6 - \Delta f_8$, and $\Delta Z_1/Z_1 - \Delta Z_3/Z_3$ are Hz, 10 Hz, and 0.1%, respectively. The resonant frequencies and impedances decrease with the increase of the (*E*)-2-hexenal concentration. The responses are not linear as a function of (*E*)-2-hexenal concentration. Then the average sensitivity in the range of (*E*)-2-hexenal concentration from 0 to 10 ppm was taken as the sensitivity when the (*E*)-2-hexenal concentration is near zero. **Figure S21**

shows fluctuations of the resonant frequencies of the sensor operated at the third-order and seventh-order modes activated by specific groups of top electrodes. The LOD of the VSA to (*E*)-2-

hexenal was determined using the value of $3\sigma/S$. **Table S6** lists the LODs of the VSA to (*E*)-2-hexenal based on multiple parameters.

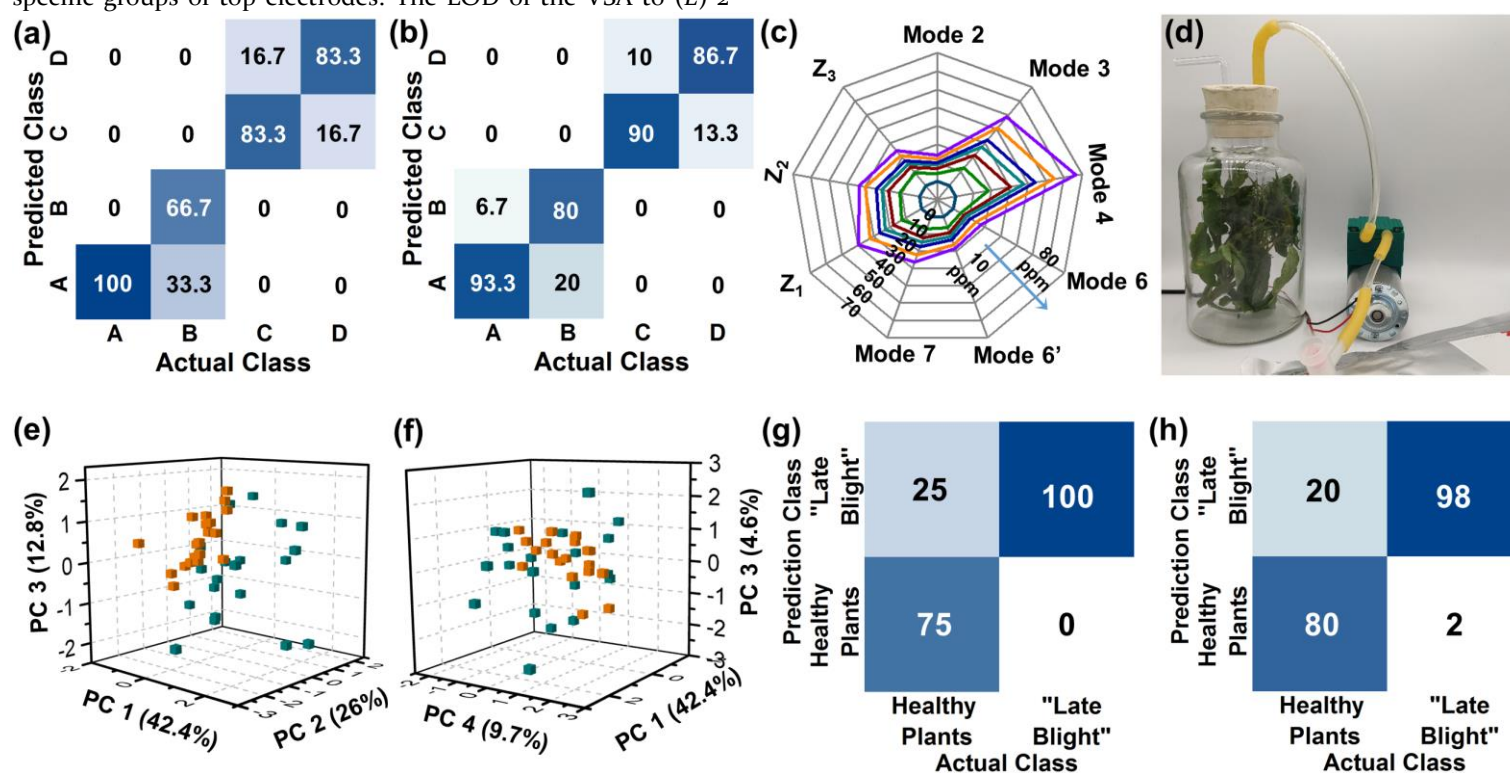


Figure 6. Identifications of VOC mixtures for diagnosis of plant diseases. LOOCV results of the identifications by the ANN model for the (a) raw data set and (b) amplified data set of the VOC mixtures. (c) Responses of the proposed VSA to (*E*)-2-hexenal. (d) Photograph of collecting emission samples from tomato leaves. 3D plot for PCA scores of the (e) first three PCs as well as (f) PC1, PC4, and PC5 from responses to two types of emissions. LOOCV results of the identifications by the ANN model for the (g) raw data set and (h) amplified data set of the responses to the plant emissions.

As shown in Table S6, the LOD of the VSA to (*E*)-2-hexenal is lower than 7.4 ppm, which is lower than the threshold value of the biomarker for late blight.⁷

Gaseous emissions of tomato leaves and potato tubers were collected, as illustrated in **Figures 6d** and **S22**. Then the VSA was used to identify the emissions from healthy plants and “plants with late blight”, which are detailed in the experimental section. The responses of the VSA to the two types of emissions were firstly analyzed by PCA. **Figures 6e** and **6f** show the 3D plots of PCA results for PC1-PC3 and PC1, PC4&5, respectively. The orange points denote the results for emissions from “plants with late blight”. Some emissions from “plants with late blight” cannot be distinguished from those of healthy plants. The ANN model was then trained for 100 times to identify the different emissions and the raw data set was amplified by 5 times from 40 to 200 data points. The amplified data set was randomly divided into a training set and a test set, containing 150 and 50 data, respectively. After training using the training set, the identification accuracy of the ANN for the test set is 78%. **Figures 6g** and **6h** show the LOOCV results for the identification of the two types of emissions using the ANN model for the raw data set and amplified data set, respectively. The results show validation accuracies of 87.5% and 89%, respectively, revealing that the piezoelectric cantilever-based VSA has great potentials for diagnosis of infectious plant diseases.

CONCLUSIONS

In conclusion, we proposed a VSA based on an AlN piezoelectric cantilever resonator with five groups of top electrodes for identification of VOCs. The amplitudes of the resonance peaks for multiple modes were enhanced by applying different groups of top electrodes for the cantilever resonator, thus achieving improved LODs of the sensor to VOCs. The multidimensional responses of the VSA to VOCs generate a unique fingerprint for each VOC and

have shown a good linearity in multidimensional space. Based on machine learning algorithms, the identification accuracies for VOCs and VOCs mixtures are 95.8% and 87.5%, respectively. Furthermore, the proposed VSA has the capacity to identify the emissions from healthy plants and “plants with late blight” with an accuracy of 89%. The high-level identifications illustrate the great potentials of the proposed VSA for diagnosis of infectious plant diseases at early stages.

ASSOCIATED CONTENT

Supporting Information. Material characterizations methods; data analysis methods; schematic illustrations of the VOC sensor, fabrication process, and VOCs sensing system; 3D model for the FEA simulation; optical and SEM images of the sensor; supplementary experimental details and results.

NOTES

The authors declare no competing financial interest.

ACKNOWLEDGMENT

This work is supported by the “National Key R&D Program of China (2018YFC0114900)”, the “Zhejiang Provincial Natural Science Foundation of China (LZ19E050002)”, the “National Natural Science Foundation of China (NSFC 51875521, 52175552)”, the “Science Fund for Creative Research Groups of National Natural Science Foundation of China (51821093)”, the Engineering Physics and Science Research Council of UK (EPSRC 10 EP/P018998/1), and International Exchange Grant (IEC/NSFC/201078) through Royal Society UK and the NSFC.

REFERENCES

- (1) Kim, I.; Kim, W.-S.; Kim, K.; Ansari, M. A.; Mehmood, M. Q.; Badloe, T.; Kim, Y.; Gwak, J.; Lee, H.; Kim, Y.-K.; et al. Holographic metasurface gas sensors for instantaneous visual alarms. *Sci. Adv.* **2021**, 7, No. eabe9943.

- (2) Jo, Y. K.; Jeong, S.-Y.; Moon, Y. K.; Jo, Y.-M.; Yoon, J.-W.; Lee, J.-H. Exclusive and ultrasensitive detection of formaldehyde at room temperature using a flexible and monolithic chemiresistive sensor. *Nat. Commun.* **2021**, *12*, No. 4955.
- (3) Potyrailo, R. A.; Go, S.; Sexton, D.; Li, X.; Alkadi, N.; Kolmakov, A.; Amm, B.; St-Pierre, R.; Scherer, B.; Nayeri, M.; et al. Extraordinary performance of semiconducting metal oxide gas sensors using dielectric excitation. *Nat. Electron.* **2020**, *3*, 280–289.
- (4) Li, Z.; Liu, Y.; Hossain, O.; Paul, R.; Yao, S.; Wu, S.; Ristaino, J. B.; Zhu, Y.; Wei, Q. Real-time monitoring of plant stresses via chemiresistive profiling of leaf volatiles by a wearable sensor. *Matter* **2021**, *4*, 2553–2570.
- (5) Lee, G.; Wei, Q.; Zhu, Y. Emerging Wearable Sensors for Plant Health Monitoring. *Adv. Funct. Mater.* **2021**, No. 2106475.
- (6) Giraldo, J. P.; Wu, H.; Newkirk, G. M.; Kruss, S. Nanobiotechnology approaches for engineering smart plant sensors. *Nat. Nanotechnol.* **2019**, *14*, 541–553.
- (7) Li, Z.; Paul, R.; Ba Tis, T.; Saville, A. C.; Hansel, J. C.; Yu, T.; Ristaino, J. B.; Wei, Q. Non-invasive plant disease diagnostics enabled by smartphone-based fingerprinting of leaf volatiles. *Nat. Plants* **2019**, *5*, 856–866.
- (8) Ren, Z.; Xu, J.; Le, X.; Lee, C. Heterogeneous Wafer Bonding Technology and Thin-Film Transfer Technology-Enabling Platform for the Next Generation Applications beyond 5G. *Micromach.* **2021**, *12*, No. 946.
- (9) Haroun, A.; Le, X.; Gao, S.; Dong, B.; He, T.; Zhang, Z.; Wen, F.; Xu, S.; Lee, C. Progress in micro/nano sensors and nanoenergy for future AIoT-based smart home applications. *Nano Express* **2021**, *2*, No. 022005.
- (10) Le, X.; Shi, Q.; Vachon, P.; Ng, E. J.; Lee, C. Piezoelectric MEMS—evolution from sensing technology to diversified applications in the 5G/Internet of Things (IoT) era. *J. Micromech. Microeng.* **2021**, *32*, No. 014005.
- (11) Clément, P.; Del Castillo Perez, E.; Gonzalez, O.; Calavia, R.; Lucat, C.; Llobet, E.; Debéda, H. Gas discrimination using screen-printed piezoelectric cantilevers coated with carbon nanotubes. *Sens. Actuators, B* **2016**, *237*, 1056–1065.
- (12) Bao, Y.; Xu, P.; Cai, S.; Yu, H.; Li, X. Detection of volatile-organic-compounds (VOCs) in solution using cantilever-based gas sensors. *Talanta* **2018**, *182*, 148–155.
- (13) Moon, H. G.; Jung, Y.; Han, S. D.; Shim, Y.-S.; Shin, B.; Lee, T.; Kim, J.-S.; Lee, S.; Jun, S. C.; Park, H.-H.; et al. Chemiresistive Electronic Nose toward Detection of Biomarkers in Exhaled Breath. *ACS Appl. Mater. Interfaces* **2016**, *8*, 20969–20976.
- (14) Fahad, H. M.; Shiraki, H.; Amani, M.; Zhang, C.; Hebbbar, V. S.; Gao, W.; Ota, H.; Hettick, M.; Kiriya, D.; Chen, Y.-Z.; et al. Room temperature multiplexed gas sensing using chemical-sensitive 3.5-nm-thin silicon transistors. *Sci. Adv.* **2017**, *3*, No. e1602557.
- (15) Lichtenstein, A.; Havivi, E.; Shacham, R.; Hahamy, E.; Leibovich, R.; Pevzner, A.; Krivitsky, V.; Davivi, G.; Presman, I.; Elnathan, R.; et al. Supersensitive fingerprinting of explosives by chemically modified nanosensors arrays. *Nat. Commun.* **2014**, *5*, No. 4195.
- (16) Thai, N. X.; Tonezzer, M.; Masera, L.; Nguyen, H.; Duy, N. V.; Hoa, N. D. Multi gas sensors using one nanomaterial, temperature gradient, and machine learning algorithms for discrimination of gases and their concentration. *Anal. Chim. Acta* **2020**, *1124*, 85–93.
- (17) Yu, Y.; Joshi, P. C.; Wu, J.; Hu, A. Laser-Induced Carbon-Based Smart Flexible Sensor Array for Multiflavors Detection. *ACS Appl. Mater. Interfaces* **2018**, *10*, 34005–34012.
- (18) Krivetskiy, V. V.; Andreev, M. D.; Efitorov, A. O.; Gaskov, A. M. Statistical shape analysis pre-processing of temperature modulated metal oxide gas sensor response for machine learning improved selectivity of gases detection in real atmospheric conditions. *Sens. Actuators, B* **2021**, *329*, No. 129187.
- (19) Li, D.; Liu, G.; Zhang, Q.; Qu, M.; Fu, Y. Q.; Liu, Q.; Xie, J. Virtual sensor array based on MXene for selective detections of VOCs. *Sens. Actuators, B* **2021**, *331*, No. 129414.
- (20) Speller, N. C.; Siraj, N.; McCarter, K. S.; Vaughan, S.; Warner, I. M. QCM virtual sensor array: Vapor identification and molecular weight approximation. *Sens. Actuators, B* **2017**, *246*, 952–960.
- (21) Potyrailo, R. A.; Bonam, R. K.; Hartley, J. G.; Starkey, T. A.; Vukusic, P.; Vasudev, M.; Bunning, T.; Naik, R. R.; Tang, Z.; Palacios, M. A.; et al. Towards outperforming conventional sensor arrays with fabricated individual photonic vapour sensors inspired by Morpho butterflies. *Nat. Commun.* **2015**, *6*, No. 7959.
- (22) Li, D.; Xie, Z.; Qu, M.; Zhang, Q.; Fu, Y.; Xie, J. Virtual Sensor Array Based on Butterworth–Van Dyke Equivalent Model of QCM for Selective Detection of Volatile Organic Compounds. *ACS Appl. Mater. Interfaces* **2021**, *13*, 47043–47051.
- (23) Speller, N. C.; Siraj, N.; Regmi, B. P.; Marzoughi, H.; Neal, C.; Warner, I. M. Rational Design of QCM-D Virtual Sensor Arrays Based on Film Thickness, Viscoelasticity, and Harmonics for Vapor Discrimination. *Anal. Chem.* **2015**, *87*, 5156–5166.
- (24) Zhao, Y.; Yang, Q.; Chang, Y.; Qu, H.; Pang, W.; Zhang, H.; Duan, X. Detection and discrimination of volatile organic compounds using a single multi-resonance mode piezotransduced silicon bulk acoustic wave resonator (PSBAR) as virtual sensor array. *Sens. Actuators B* **2018**, *254*, 1191–1199.
- (25) Le, X.; Peng, L.; Pang, J.; Xu, Z.; Gao, C.; Xie, J. Humidity sensors based on AlN microcantilevers excited at high-order resonant modes and sensing layers of uniform graphene oxide. *Sens. Actuators, B* **2019**, *283*, 198–206.
- (26) Li, D.; Dong, H.; Xie, Z.; Zhang, Q.; Qu, M.; Fu, Y.; Xie, J. High Resolution and Fast Response of Humidity Sensor Based on AlN Cantilever with Two Groups of Segmented Electrodes. *IEEE Electron Device Lett.* **2021**, *42*, 923–926.
- (27) Li, D.; Shao, Y.; Zhang, Q.; Qu, M.; Ping, J.; Fu, Y.; Xie, J. A flexible virtual sensor array based on laser-induced graphene and MXene for detecting volatile organic compounds in human breath. *Analyst* **2021**, *146*, 5704–5713.
- (28) Jiang, G.; Golezdzinowski, M.; Comeau, F. J. E.; Zarrin, H.; Lui, G.; Lenos, J.; Veileux, A.; Liu, G.; Zhang, J.; Hemmati, S.; et al. Free-Standing Functionalized Graphene Oxide Solid Electrolytes in Electrochemical Gas Sensors. *Adv. Funct. Mater.* **2016**, *26*, 1729–1736.
- (29) Xu, B.; Huang, J.; Xu, X.; Zhou, A.; Ding, L. Ultrasensitive NO Gas Sensor Based on the Graphene Oxide-Coated Long-Period Fiber Grating. *ACS Appl. Mater. Interfaces* **2019**, *11*, 40868–40874.
- (30) Zhang, C.; Hou, Z.-L.; Zhang, B.-X.; Fang, H.-M.; Bi, S. High sensitivity self-recovery ethanol sensor based on polyporous graphene oxide/melamine composites. *Carbon* **2018**, *137*, 467–474. DOI: <https://doi.org/10.1016/j.carbon.2018.05.055>.
- (31) Xu, Z.; Sun, H.; Zhao, X.; Gao, C. Ultrastrong Fibers Assembled from Giant Graphene Oxide Sheets. *Adv. Mater.* **2013**, *25*, 188–193.
- (32) Medhekar, N. V.; Ramasubramaniam, A.; Ruoff, R. S.; Shenoy, V. B. Hydrogen Bond Networks in Graphene Oxide Composite Paper: Structure and Mechanical Properties. *ACS Nano* **2010**, *4*, 2300–2306.
- (33) Zhu, Y.; Murali, S.; Cai, W.; Li, X.; Suk, J. W.; Potts, J. R.; Ruoff, R. S. Graphene and Graphene Oxide: Synthesis, Properties, and Applications. *Adv. Mater.* **2010**, *22*, 3906–3924.
- (34) Tonezzer, M.; Kim, J.-H.; Lee, J.-H.; Iannotta, S.; Kim, S. S. Predictive gas sensor based on thermal fingerprints from Pt-SnO₂ nanowires. *Sens. Actuators, B* **2019**, *281*, 670–678.
- (35) Tonezzer, M.; Le, D. T. T.; Iannotta, S.; Van Hieu, N. Selective discrimination of hazardous gases using one single metal oxide resistive sensor. *Sens. Actuators B* **2018**, *277*, 121–128.
- (36) Dimiev, A. M.; Tour, J. M. Mechanism of Graphene Oxide Formation. *ACS Nano* **2014**, *8*, 3060–3068.
- (37) Yeh, C.-N.; Raidongia, K.; Shao, J.; Yang, Q.-H.; Huang, J. On the origin of the stability of graphene oxide membranes in water. *Nat. Chem.* **2015**, *7*, 166–170.
- (38) Bian, Y.; Bian, Z.-Y.; Zhang, J.-X.; Ding, A.-Z.; Liu, S.-L.; Wang, H. Effect of the oxygen-containing functional group of graphene oxide on the aqueous cadmium ions removal. *Appl. Surf. Sci.* **2015**, *329*, 269–275.
- (39) Wang, T.; Lee, C. Electrically switchable multi-frequency piezoelectric micromachined ultrasonic transducer (pMUT). In *2016 IEEE 29th Int. Conf. on Micro Electro Mech. Syst. (MEMS)*, 24–28 Jan. 2016, 2016; pp 1106–1109.
- (40) Li, D.; Le, X.; Pang, J.; Xie, J. An ALN Resonant Microcantilever Humidity Sensor by Activating Specific Sets of Top Electrodes Based on Graphene Oxide. In *2019 20th Int. Conf. on Solid-State Sens., Actuators and Microsys. & Eurosens. XXXIII (TRANSDUCERS & EUROSensors XXXIII)*, 23–27 June 2019, 2019; pp 1337–1340.
- (41) Chen, W.; Deng, F.; Xu, M.; Wang, J.; Wei, Z.; Wang, Y. GO/Cu₂O nanocomposite based QCM gas sensor for trimethylamine detection under low concentrations. *Sens. Actuators, B* **2018**, *273*, 498–504.
- (42) Yang, Y.; Li, S.; Yang, W.; Yuan, W.; Xu, J.; Jiang, Y. In Situ Polymerization Deposition of Porous Conducting Polymer on Reduced Graphene Oxide for Gas Sensor. *ACS Appl. Mater. Interfaces* **2014**, *6*, 13807–13814.
- (43) Le, X.; Wang, X.; Pang, J.; Liu, Y.; Fang, B.; Xu, Z.; Gao, C.; Xu, Y.; Xie, J. A high performance humidity sensor based on surface acoustic wave and

graphene oxide on AlN/Si layered structure. *Sens. Actuators, B* **2018**, 255, 2454-2461.

(44) Gao, F.; Xuan, W.; Bermak, A.; Boussaid, F.; Tsui, C.-Y.; Luo, J. Dual transduction on a single sensor for gas identification. *Sens. Actuators, B* **2019**, 278, 21-27.

